Real time monitoring of radiofrequency ablation based on MR thermometry and thermal dose in the pig liver in vivo

Olivier Seror, Matthieu Lepetit-Coiffé, B. Le Bail, Baudouin Denis de Senneville, Hervé Trillaud, Chrit T. W. Moonen, Bruno Quesson

HAL Id: hal-01065595
https://hal.science/hal-01065595

Submitted on 28 Dec 2017

Olivier Seror
Matthieu Lepetit-Coiffé
Brigitte Le Bail
Baudouin Denis de Senneville
Hervé Trillaud
Chrit Moonen
Bruno Quesson

Real time monitoring of radiofrequency ablation based on MR thermometry and thermal dose in the pig liver in vivo

O. Seror · M. Lepetit-Coiffé ·
B. D. de Senneville · H. Trillaud ·
C. Moonen · B. Quesson
Imagerie Moléculaire et Fonctionnelle:
de la physiologie à la thérapie, ERT
CNRS/Université Victor Segalen
Bordeaux 2,
33000 Bordeaux, France

B. Le Bail
Service d'Anatomopathologie Hôpital
Pellegrin, CHU Bordeaux,
33000 Bordeaux, France

O. Seror (✉)
Service de Radiologie Hôpital Jean
Verdier, Assistance Publique-Hôpitaux
de Paris/CHU Paris XIII,
avenue du 14 Juillet,
93140 Bondy, France
e-mail: olivier.seror@jvr.aphp.fr
Tel.: +33-1-48026071
Fax: +33-1-48026053

H. Trillaud
Service de Radiologie, Hôpital Saint-
André, CHU Bordeaux,
33000 Bordeaux, France

Abstract To evaluate the feasibility and accuracy of MR thermometry based on the thermal dose (TD) concept for monitoring radiofrequency (RF) ablations, 13 RF ablations in pig livers were performed under continuous MR thermometry at 1.5 T with a filtered clinical RF device. Respiratory gated fast gradient echo images were acquired simultaneously to RF deposition for providing MR temperature maps with the proton resonant frequency technique. Residual motion, signal to noise ratio (SNR) and standard deviation (SD) of MR temperature images were quantitatively analyzed to detect and reject artifacted images in the time series. SD of temperature measurement remained under 2°C. Macroscopic analysis of liver ablations showed a white zone (Wz) surrounded by a red zone (Rz). A detailed histological analysis confirmed the ongoing nature of the coagulation necrosis in both Wz and Rz. Average differences (±SD) between macroscopic size measurements of Wz and Rz and TD predictions of ablation zones were 4.1 (±1.93) mm and −0.71 (±2.47) mm, respectively. Correlation values between TD and Wz and TD and Rz were 0.97 and 0.99, respectively. MR thermometry monitoring based on TD is an accurate method to delineate the size of the ablation zone during the RF procedure and provides a clinical endpoint.

Keywords Radiofrequency ablation ·
Magnetic resonance imaging ·
MR thermometry · Thermal dose ·
Interventional procedures

Abbreviations RF: radiofrequency ·
TD: thermal dose · PRF: proton
resonance frequency · Wz: white zone
of ablation zone at macroscopic
inspection · Rz: white and red zones
of ablation zone at macroscopic
inspection

Introduction

Hyperthermal ablation therapies for the treatment of malignant liver tumor have gained popularity, especially radiofrequency (RF) because of the relative simplicity and low cost of its instrumentation [1]. Although the safety [2–4] and effectiveness [1] of RF have been widely investigated, the current lack of reliable continuous real time imaging for monitoring the procedure is an important limitation to broaden the spectrum of its indications [5, 6]. The assessment of treatment efficiency with computed tomography (CT) or magnetic resonance (MR) imaging requires intravenous injection of extra-cellular non-specific contrast agents, which are restricted to a single injection after completion of the ablation procedure. Recently, contrast enhancement ultrasonography (US) using new

microbubble contrast agents has been suggested to be effective for immediate post-procedure delimitation of the ablation zone [7], but was found to be of limited sensitivity (about 30%) for detecting residual tumor at 24 h [8]. However, although few consecutive injections of US contrast agent can be performed during a RF ablation procedure, this method does not provide the operator a real time and quantitative monitoring of the thermal ablation.

Several years ago, Sapareto et al. introduced the thermal dose (TD) concept suggesting a strong relationship between cell death, temperature rise and exposition time [9]. More recently, two studies using different methodological approaches [10, 11] estimated a lethal temperature threshold around 55°C for short treatment times (less than 5 min), which was consistent with the TD concept. Thus, real time calculation of the TD map from dynamic MR temperature images [12–15] is expected to be particularly suitable for monitoring hyperthermal ablations. In addition, this technique should allow a monitoring of thermal ablation on large tumors (3 cm or more in diameter) where several overlapping RF ablations are required. Moreover, MR thermometry during RF ablation is possible with an efficient filtering of electromagnetic interferences induced by RF devices [16–18]. However, MR thermometry for monitoring RF ablation in mobile organs such as the liver remains to be fully investigated concerning its ability to provide relevant and accurate size estimations of ablation zones based on TD calculation.

For this purpose, we designed a preclinical in vivo study of MR thermometry for monitoring RF ablations performed in the liver of pig with clinical RF and MR instrumentations to evaluate the feasibility and the precision of TD delineation of the ablation zones and to confirm the ability of novel image processing methods to improve the quality of temperature imaging. In this study, we investigated if the resulting quantitative and non-invasive measurement of the TD from dynamic MR temperature images can provide a reliable clinical endpoint for the ablation procedure.

Materials and methods
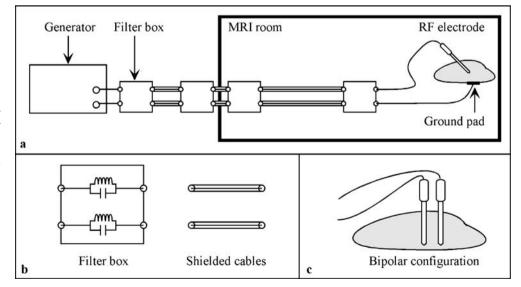
Animal preparation

All procedures were performed in accordance with the National Institutes of Health guidelines for care and use of laboratory animals and with the approval of the committee of animal research of our institution.

Four male pigs (weight range, 40–65 kg) were given an intramuscular injection (5 mg/kg) of ketamine (Ketalar®, Pfizer, Paris, France) for induction of anaesthesia. The animals were placed in a 1.5-T clinical MR unit (Intera; Philips Medical System, Best, the Netherlands) in dorsal decubitus position, and the abdomen was surrounded by a four-element flexible phased-array coil dedicated to abdominal imaging. Then, a mixture of 2% isoflurane (Isoflurane Belamont®, Limburg, Germany) in air was continuously administered for maintenance of general anesthesia. Monitoring of vital parameters included cardiac and respiratory frequency recording and intra-rectal temperature measurements.

RF ablation

All RF ablation experiments (n=13) were performed using a clinical RF device (Tyco Healthcare/ Radionics, Burlington, MA) operating at a 480-kHz frequency with 100 watts of maximum output power. A MR-compatible

Fig. 1 Schematic view of the hardware design for simultaneous RF ablation and MR temperature imaging. (**a**) General view of the monopolar configuration: the output of the generator is filtered by several filter boxes outside and (**b**) inside the MRI room. Each filter box contains rejection filters for each line of the transmission, consisting of inductors and capacitors arranged in parallel, and shielded cables are used to avoid electromagnetic interferences to perturb the MR signal. (**c**) In the bipolar configuration, the ground pad is replaced by the second electrode inserted into the liver

RF electrode of 15-cm length and 17-gauge (1.15 mm) in diameter was internally cooled with sterile water maintained at 4° C using a peristaltic pump (Cool Tip®, Radionics/Valley Lab/Tyco CC-1; Boulder, CO). The RF generator and peristaltic pump were placed outside the MR room. The electrically active part of the electrode tip was 3 cm in length, and a MR-compatible grounding pad of 1,000 cm^2 was stuck on the skin of the pig thigh. Eleven monopolar and two bipolar RF ablations were performed. For the latter configuration, a second identical electrode was inserted parallel to the first one at a distance of 2.5 to 3 cm and connected to the electrical circuit instead of the ground pad.

The output signal of the generator was filtered with passive stop band filters (Fig. 1). The resulting maximal attenuation at the Larmor frequency at 1.5 T (64 MHz) was measured to be more than 90dB. The output power of the generator measured on a 100 Ohms resistive load was found to be identical in the presence and absence of the filters.

Positioning of the electrode(s) was performed after acquiring coronal and transverse balance-FFE images of the complete abdomen. Then, RF energy was applied for 12 min at maximal available output power (routine protocol with this device [4]).

MR thermometry

Temperature images were calculated with the PRF (coefficient −0.094 ppm/°C) shift technique [19]. A water-selective binomial excitation was combined with a segmented gradient echo planar imaging (EPI) sequence [20]. Respiratory motion was compensated by gating acquisition on the expiration phase of the respiratory cycle using a pressure sensor taped on the abdomen of the animal. Three slices of 5 mm thick with 0.6 mm gap were acquired with the following parameters: TE/TR/flip angle (FA): 14ms/260ms/40°, 9 echoes/TR, FOV: 240×240 mm, matrix: 128×108 (zero-filled to 128×128), left-right phase-encode direction, acquisition time: 3.2s/volume, in plane resolution (IPR): 1.9×2.2 mm. Continuous image acquisition was performed before (2.5 min), during (12 min) and after (2 min) RF energy deposition.

Image processing for temperature imaging

Magnitude and phase images were transferred online from the MRI scanner to a separate workstation dedicated to temperature imaging (Thermoguide, Image guided therapy SA, Pessac, France). This software allowed for calculation and display (100 ms/slice processing time) of temperature from phase and of TD maps (according to Sapareto et al.'s equation [9]). The threshold value for TD was set equivalent to a reference dose corresponding to 43°C during 240 min [19].

Post processing

A decreased SNR due to incomplete filtering and to possible residual organ displacements may occur and thereby increase the standard deviation of temperature estimation [21]. Therefore, additional image processing was performed off-line as follows [22]: first, in each pixel of a ROI located outside the heated region, the standard deviation of the MR temperature measurements was calculated before, during and after RF ablation; second, residual motion was corrected using an atlas of reference data (magnitude and corresponding phase images) for the different liver positions recorded before the heating phase; third, if the temperature standard deviation (outside the RF ablation zone) following the above-mentioned correction exceeded 10% of a predefined maximal value, the temperature image was removed from the TD calculation process.

Assessment of feasibility of RF ablation monitoring by MR thermometry

Duration of the procedure from animal positioning to the last MRI acquisition was systematically recorded. The electrical parameters of each RF ablations (voltage, current intensity, output power and tissue impedance) were recorded (Radionics software) to calculate the deposited energy.

Dimension of the susceptibility artifact induced by the RF electrode was measured on the magnitude image of the thermometry sequence. Signal-to-noise ratio (SNR) of magnitude images measured during the RF ablation were compared to initial SNR prior to RF energy deposition to estimate the efficiency of filtering using the following equation [23]:

$$SNR = S \cdot \sqrt{2 - \pi/2} \Big/ N$$

where S is the average value of the magnitude image in a ROI located in the liver, and N is the standard deviation of noise measured in a ROI outside the animal.

Assessment of MR thermometry accuracy

Without knowledge of the histopathological results, small axis measurements on TD images (without image magnification) for each RF ablation zone were performed by the same observers (O.S., M.L.-C. and B.Q.) at the end of the RF procedure. Small axis measurement was chosen as study parameter, since (1) transversal size of the ablation zone is known to be the main restrictive limitation of the RF treatment in clinical practice and (2) due to the landmark of the electrode path, its measurement is the most reproducible both on image and specimen.

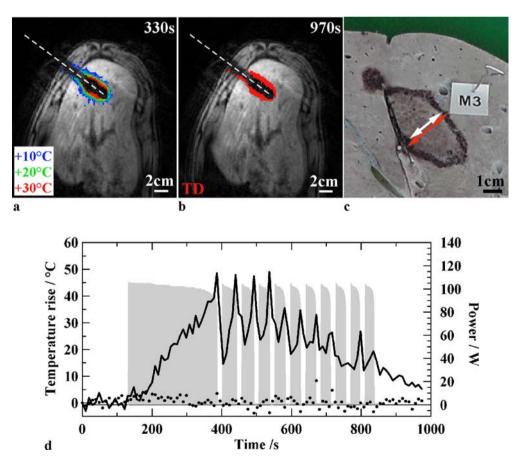## Liver gross pathologic and histopathological evaluations

After completion of the ablations, each animal was immediately sacrificed with an intravenous injection (200 mg/kg) of sodium pentobarbital, and the liver was removed. The main trunk of the portal vein was immediately catheterized with a large canula, and the liver vasculature was washed with a 9/1,000 NaCl solution, and thereafter perfusion-fixed with 10% formaldehyde. After 2 weeks of fixation, the livers were sliced in axial plane every 3–5 mm. Electrode position was determined in each ablation zone using the central burn hole as a landmark. In accordance with previous reports [24, 25], ablation zones exhibited a typical pattern having a central "white zone" (Wz) surrounded by a peripheral "red zone" (Rz). Thus, for each ablation zone, the two largest small diameters perpendicular to the electrode axis were measured: the smaller one, including exclusively the Wz, and the largest one, including both Wz and Rz. These ex vivo measurements were performed by the pathologist (B.L.B.) without prior knowledge of the MR imaging results and were corrected for the retraction factor of 10% due to formalin fixation. This retraction factor was experimentally determined by multiple measures of 10-cm lines of tissue before and after 2 weeks fixation.

Tissue samples were then embedded in paraffin for routine histological analysis: 5-μm thick sections were stained with hematoxylin-eosin-saffron (HES) for evaluation of tissue damage, and with Gordon-Sweets reticulin stain for evaluation of the preservation of extra-cellular matrix. Immunostaining with a mouse monoclonal antibody antihepatocyte (Clone M7158, DakoCytomation, Glostrup, DK) diluted at 1/50 was performed on paraffin sections after heat-induced antigen retrieval. This antibody is specific for mitochondrial epitope in human hepatocyte, but also reacts with pig hepatocytes [26].

Statistical analysis

Statistical relationship between paired transverse axis measurements between TD and histopathological results (Rz and Wz) taken as a gold standard was studied with the Pearson's linear correlation ("R" value). In addition, the Bland and Altman graphical method [27] was used to identify a potential relationship between the differences in size between TD and Rz or Wz, respectively, and to detect systematic bias in measurements, and the presence of possible measurements outside of the 95% confidence interval.

Fig. 2 Typical results of a RF ablation in pig liver. (**a**) Gray-scale magnitude image obtained 330 s after the beginning of RF ablation, with superimposed temperature increases indicated with color code levels (blue corresponds to +10°C, green to +20°C and red to +30°C above starting physiological temperature); RF electrode actual size is indicated by the white dashed line in the middle of the susceptibility artifact. (**b**) Thermal dose map (TD) superimposed on magnitude image obtained at the end of the RF ablation procedure. Red pixels indicate region were lethal dose was reached. (**c**) Macroscopic slice of the liver after fixation. White and red arrows stand for white (Wz) and red (Rz) zones largest small diameters measurements perpendicular to the electrode axis. (**d**) Temporal evolution of temperature for two pixels located at 10 mm (black continuous line) and 40 mm distance from the RF electrode (black dotted line), respectively. Duration of effective RF power deposition is indicated in gray

Results

Feasibility of RF ablation monitoring by MR thermometry

Duration of each experiment ranged from 4 h to 7 h (mean: 6 h; 30 min/RF ablation). No animal experienced alteration of vital parameters, and no skin burn was shown at post-procedure inspection.

The amount of total RF energy deposition for the 13 RF ablations ranged from 56 kJ to 84 kJ (mean ± SD: 69± 10 kJ), and the number of impedance rises detected by the generator varied from 0 to 12 (mean ± SD: 4.3±4.8). Typical results from a MRI-guided RF ablation on a pig

liver are displayed on Fig. 2. On TD images, the thickness of susceptibility artifact induced by the electrode was 15 mm±2 mm.

SNR values ranged from 29 to 90 (mean ± SD: 46±26) before ablation and from 20 to 80 (mean ± SD: 41±23) during RF deposition. The threshold for detecting the presence of an artifacted image was set to 2°C (see Materials and Methods).

During RF energy deposition and without applying the image processing, the standard deviation of temperature maps ranged from 1.3°C to 3.57°C (mean 2.56°C±1.3°C). After correction, it ranged from 1.1°C to 2.44°C (mean 1.7°C±0.37°C). For one experiment only, the temperature images could not be exploited without motion compensa-
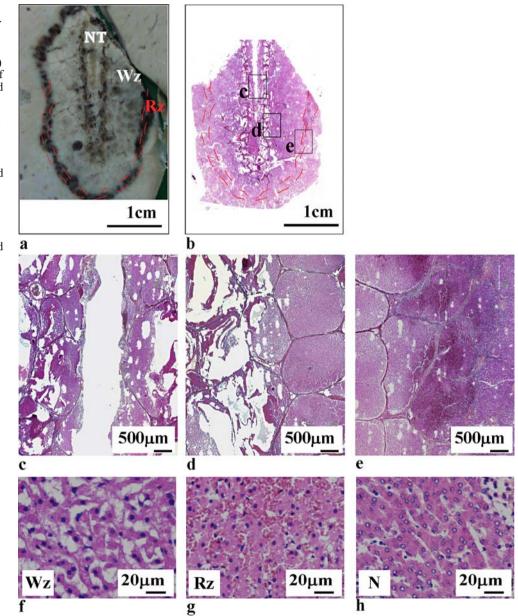
Fig. 3 Macroscopic and histological (HES staining) slices of the lesion created by a RF ablation. (**a**) Macroscopic slice on which the needle track (NT) clearly appears in the middle of the white zone (Wz), surrounded by the red zone (Rz, dashed lines). (**b**) General histological view from which the characteristic zoning is extracted. (**c**) Both sides of the RF needle track. (**d**) Border between RF needle track and white zone and (**e**) border between white zone, red zone and the untreated tissue. Images (**f**), (**g**) and (**h**) are zoomed views of the Wz, Rz and untreated tissue, respectively. NT: needle track, Rz: red zone, Wz: white zone, N: untreated tissue (normal liver)

tion. For all the 13 experiments, less than 10% (in the worst case) of images in the time series were finally removed because of the standard deviation of temperature measurements exceeding the threshold of 2°C. A more detailed analysis of these removed images revealed that they all corresponded to sudden impedance rises presumably at the origin of broadband electromagnetic emission interfering with MR thermometry as previously reported [16]. No other temperature images had to be removed, indicating that combining respiratory gating with atlas-based correction technique was sufficient to keep the accuracy of temperature measurement within 2°C.

RF lesion dimensions

At gross pathologic examination of fixed tissues (Fig. 2), all thermal ablation zones were clearly visible and appeared ovoid, with an ellipsoid shape on sections. The electrode shaft systematically appeared as a central, small and black hole, surrounded by a large central Wz contoured by a continuous dark red ring of 1 mm to 4 mm thick, corresponding to the Rz. The long axis of thermal ablation zones grossly corresponded to the length of the active tip of the electrode. Histopathological study of the ablation zone

revealed the three zones (electrode shaft, Wz and Rz) (Fig. 3). At the microscopic level, tissue alterations in the Wz and Rz, as compared with normal liver, appeared less obvious than at the macroscopic level. However, in the Wz, hepatocytes appeared polygonal and enlarged, with hypereosinophilic cytoplasms, hyperbasophilic nuclei and undefined cytoplasmic limits (Fig. 3f). In the Rz (Fig. 3g), cells tended to be round and smaller, uncohesive, dissociated by hemorrage, with hyperchromatic and pycnotic nuclei and hypereosinophilic cytoplasms. This was suggestive of ongoing coagulative necrosis in both zones. Reticulin stain (Fig. 4) showed the complete or partial disappearance of the matricial sinusoidal network in the Rz and Wz (Fig. 4b–c), as compared to normal tissue (Fig. 4a). The cytoplasmic staining of hepatocytes with anti-hepatocyte antibody, a marker of the mitochondrial fraction of hepatocytes [26], was negative in Rz and Wz (Fig. 4f–g), contrasting with the strong staining of normal hepatocytes (Fig. 4e). These two results, in addition to basic histology analysis, were suggestive of fatal cell, matricial and mitochondrial alterations in both Rz and Wz.

RF ablation dimensions performed with a single electrode (n=11) ranged from 17.6 mm to 30.8 mm for the Wz (mean 21.15±3.87 mm) and from 22 mm to 37.4 mm for the Rz (mean 26.25 mm±4.60 mm). For the experiments

Fig. 4 Reticulin network staining in the normal liver (a), in the red zone (b) and in the white zone (c): the extracellular matrix is gradually altered in the Rz and Wz. Immunostaining (d-g) with anti-human hepatocyte antibody: the mitochondrial epitope is detected as granular cytoplasmic staining in the normal liver (e). Staining is absent in the red zone (f) and in the white zone (g). N: untreated tissue (normal liver), Rz: red zone, Wz: white zone

performed in bipolar configuration (n=2), ablation zone sizes were 53.9 mm and 55 mm for the Wz, and 55 mm and 60.5 mm for the Rz, respectively. Correlation studies between apparent ablation zone sizes observed on TD maps and at macroscopic examination for Rz and Wz taken as a gold standard are displayed in Fig. 5. For Wz and Rz, R values were 0.99 and 0.98, with a slope of the linear regression of 0.97 ± 0.04 (Wz) and 0.99 ± 0.06 (Rz), and offset values of 4.85 mm$\pm$1.28 mm and -0.53 mm$\pm$1.97 mm, respectively.

The Bland and Altman method (Fig. 6) showed no bias depending on the ablation zone size and only one measurement was found outside the 95% confidence interval. Ablation size estimation from TD maps was larger than the Wz (4.1 ± 1.93 mm for mean $\pm$ standard deviation), but smaller than the Rz (-0.71 ± 2.47 mm).

Discussion

In addition to tumor identification, puncture guidance [28] and post-ablation assessment of thermal lesion [29, 30], MRI can provide quantitative TD images during tissue ablation [31]. The proton resonant frequency technique appears to be the most suitable method for online thermometry [12, 13, 19, 32–34], since it is nearly independent of tissue characteristics, is linear with temperature increase and is compatible with fast imaging
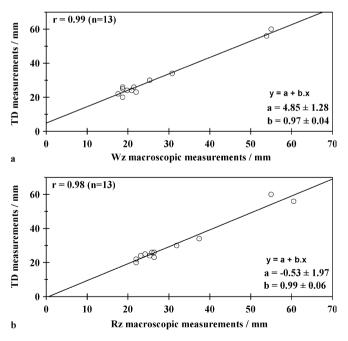
Fig. 6 Bland and Altman representation of the agreement between the dimensions of the thermal dose maps (TD) and the measurements of the dimensions of the Wz (**a**) and Rz (**b**), respectively. Numerical values of the mean differences and limits of the confidence interval (CI) are reported on the graph and represented by horizontal solid lines

Fig. 5 Pearson's linear correlations between measurements of transverse axis of the lesions (n=13) on thermal dose maps (TD) and macroscopic measurements of (**a**) the white (Wz) and (**b**) the red (Rz) zones taken as a gold standard; Pearson's correlation coefficient (r) and coefficients of the linear regression are indicated on the graphs
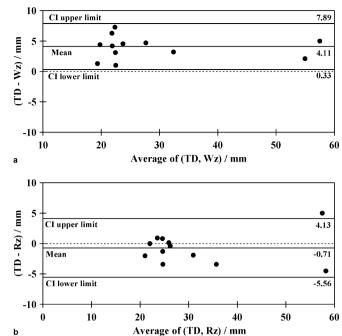
sequences. In the present study, the feasibility of quantitative MR thermometry monitoring simultaneously with radiofrequency ablation on pig liver in vivo was demonstrated using standard clinical MR and radiofrequency instrumentation. During high RF power deposition, only a slight decrease of SNR (11%) on MR images was observed, indicating that most electromagnetic interferences were effectively suppressed. Despite a slight decrease of SNR (11%) during RF deposition, the standard deviation of temperature maps remained excellent (less than 2°C). Similar results have already been reported using an experimental RF device [17] at 1.5 T and with a clinical ablation generator internally modified to operate at 0.5 T [18].

Assessment of the accuracy of MR thermometry mapping for predicting the limit of ablation zones is the second mandatory step before considering possible future clinical applications. The TD was demonstrated to be a relevant concept to delineate radiofrequency ablation performed on *ex vivo* liver [16] and in vivo on small animal model [17], but radiofrequency ablations were performed with home-made devices. MR thermometry monitoring was also reported using a commercial radiofrequency device in a large animal model, but the analysis of liver specimens did not allow an accurate assessment of the correspondence between temperature maps and actual lesion size [18]. In the present study, the experimental setup was identical to

the clinical conditions, and a strong correlation was established between lesion size predicted from TD maps and histological analysis. Note that despite the use of an identical heating protocol for each ablation, the variability of ablation zone size remained important (22 to 37.4 mm for the Rz in monopolar configuration). These variations were clearly identified on TD maps, demonstrating the usefulness of a quantitative monitoring of RF ablation.

Lesion sizes predicted from TD maps were in good agreement with macroscopic measurements of the RZ, with an average difference close to zero and a standard deviation in the range of the resolution of the thermometry sequence (see Fig. 6b). In addition, the excellent correlation between TD/Rz and TD/Wz measurements (see Fig. 5) tend to suggest that quantitative MR temperature imaging provides a precise, non-invasive and on line estimate of the actual tissular destruction, in agreement with already published results on a small animal model [17].

In the present work, the histological analysis demonstrated that tissular damage was observed in both Rz and Wz. Conventional histology was suggestive of ongoing coagulation necrosis in both the red and white zones, but the precise delineation of the microscopic lesions could not be established. However, animal sacrifice was here performed immediately after RF ablation, and thermal lesions (mostly coagulation necrosis) are more difficult to identify with certainty at the microscopic level with HES staining less than 3 days following the therapeutic intervention [35].

Additional techniques based on the detection of altered mitochondrial enzyme activities on frozen sections might be helpful to evidence the loss of mitochondrial enzymatic activity associated with cell death, but could not be performed in the present work due to the absence of frozen tissues. Therefore, two additional techniques were developed on paraffin sections to estimate the integrity of the extracellular matrix (reticulin staining) and of the mitochondrial fraction of hepatocytes (immunostaining with the M7158 antibody). Both were clearly suggestive of fatal tissular alteration on both red and white zones.

In this study, the relatively small volume coverage of TD maps could be regarded as a limitation of the method for monitoring the ablation of large tumors. Further improvements in fast MR imaging techniques to acquire more slices and/or to increase spatial resolution of the MR thermometry sequence will be helpful for widespread clinical use. Direct comparison of TD maps with conventional MR imaging, especially gadolinium enhanced T1-weighted images, would also be interesting to assess the correspondence between the two methods. However, this was not the aim of this work, and previous studies have already investigated the correspondence between gadolinium-enhanced images acquired at the end of the RF ablation and TD maps [17], suggesting that the two methods would be complementary in clinical practice. In addition, the correspondence between histology and conventional follow-up imaging has also been widely investigated [29, 30, 36, 37]. Finally, it should be noted that experiments were here performed in this study on healthy animals. Thus, the effectiveness of TD mapping remains to be evaluated quantitatively on pathological tissue.

In summary, following a standard protocol of RF energy deposition performed with a clinical RF device on a clinical 1.5-T magnet, MR thermometry based on PRF technique and the TD concept allowed an accurate monitoring of radiofrequency ablations in pig liver in vivo.

In view of future clinical application, quantitative rapid MR temperature imaging may provide the physician with an effective real-time monitoring of the intervention and a clinical endpoint for the therapeutic treatment.

References

1. Sutherland LM, Williams JA, Padbury RT, Gotley DC, Stokes B, Maddern GJ (2006) Radiofrequency ablation of liver tumors: a systematic review. Arch Surg 141:181–190
2. Mulier S, Mulier P, Ni Y, Miao Y, Dupas B, Marchal G, De Wever I, Michel L (2002) Complications of radiofrequency coagulation of liver tumours. Br J Surg 89:1206–1222
3. Rhim H, Yoon KH, Lee JM, Cho Y, Cho JS, Kim SH, Lee WJ, Lim HK, Nam GJ, Han SS, Kim YH, Park CM, Kim PN, Byun JY (2003) Major complications after radio-frequency thermal ablation of hepatic tumors: spectrum of imaging findings. Radiographics 23:123–134
4. Livraghi T, Solbiati L, Meloni MF, Gazelle GS, Halpern EF, Goldberg SN (2003) Treatment of focal liver tumors with percutaneous radio-frequency ablation: complications encountered in a multicenter study. Radiology 226:441–451
5. Leyendecker JR, Dodd GD 3rd, Halff GA, McCoy VA, Napier DH, Hubbard LG, Chintapalli KN, Chopra S, Washburn WK, Esterl RM, Cigarroa FG, Kohlmeier RE, Sharkey FE (2002) Sonographically observed echogenic response during intraoperative radiofrequency ablation of cirrhotic livers: pathologic correlation. AJR Am J Roentgenol 178:1147–1151

6. Raman SS, Lu DS, Vodopich DJ, Sayre J, Lassman C (2000) Creation of radiofrequency ablation zones in a porcine model: correlation with sonography, CT, and histopathology. AJR Am J Roentgenol 175:1253–1258

7. Solbiati L, Tonolini M, Cova L (2004) Monitoring RF ablation. Eur Radiol 14:34–42

8. Vilana R, Bianchi L, Varela M, Nicolau C, Sanchez M, Ayuso C, Garcia M, Sala M, Llovet JM, Bruix J, Bru C; BCLC Group (2006) Is microbubble-enhanced ultrasonography sufficient for assessment of response to percutaneous treatment in patients with early hepatocellular carcinoma? Eur Radiol 16 (11):2454–2462

9. Sapareto SA, Dewey WC (1984) Thermal dose determination in cancer therapy. Int J Radiat Oncol Biol Phys 10:787–800

10. Puccini S, Bar NK, Bublat M, Kahn T, Busse H (2003) Simulations of thermal tissue coagulation and their value for the planning and monitoring of laser-induced interstitial thermotherapy (LITT). Magn Reson Med 49:351–362

11. de Jode MG, Lamb GM, Thomas HC, Taylor-Robinson SD, Gedroyc WM (1999) MRI guidance of infra-red laser liver tumour ablations, utilising an open MRI configuration system: technique and early progress. J Hepatol 31:347–353

12. Peters RD, Hinks RS, Henkelman RM (1998) Ex vivo tissue-type independence in proton-resonance frequency shift MR thermometry. Magn Reson Med 40:454–459

13. Wlodarczyk W, Boroschewski R, Hentschel M, Wust P, Monich G, Felix R (1998) Three-dimensional monitoring of small temperature changes for therapeutic hyperthermia using MR. J Magn Reson Imaging 8:165–174

14. Moriarty JA, Chen JC, Purcell CM, Ang LC, Hinks RS, Peters RD, Henkelman RM, Plewes DB, Bronskill MJ, Kucharczyk W (1998) MRI monitoring of interstitial microwave-induced heating and thermal ablation zones in rabbit brain in vivo. J Magn Reson Imaging 8:128–135

15. Chen JC, Moriarty JA, Derbyshire JA, Peters RD, Trachtenberg J, Bell SD, Doyle J, Arrelano R, Wright GA, Henkelman RM, Hinks RS, Lok SY, Toi A, Kucharczyk W (2000) Prostate cancer: MR imaging and thermometry during microwave thermal ablation-initial experience. Radiology 214:290–297

16. Seror O, Lepetit-Coiffe M, Quesson B, Trillaud H, Moonen CT (2006) Quantitative magnetic resonance temperature mapping for real-time monitoring of radiofrequency ablation of the liver: an ex vivo study. Eur Radiol 16:2265–2274

17. Lepetit-Coiffe M, Quesson B, Seror O, Dumont E, Le Bail B, Moonen CT, Trillaud H (2006) Real-time monitoring of radiofrequency ablation of rabbit liver by respiratory-gated quantitative temperature MRI. J Magn Reson Imaging 24:152–159

18. Vigen KK, Jarrard J, Rieke V, Frisoli J, Daniel BL, Butts Pauly K (2006) In vivo porcine liver radiofrequency ablation with simultaneous MR temperature imaging. J Magn Reson Imaging 23:578–584

19. Quesson B, de Zwart JA, Moonen CT (2000) Magnetic resonance temperature imaging for guidance of thermotherapy. J Magn Reson Imaging 12:525–533

20. de Zwart JA, Vimeux FC, Delalande C, Canioni P, Moonen CT (1999) Fast lipid-suppressed MR temperature mapping with echo-shifted gradient-echo imaging and spectral-spatial excitation. Magn Reson Med 42:53–59

21. Boss A, Graf H, Muller-Bierl B, Clasen S, Schmidt D, Pereira PL, Schick F (2005) Magnetic susceptibility effects on the accuracy of MR temperature monitoring by the proton resonance frequency method. J Magn Reson Imaging 22:813–820

22. Denis de Senneville B, Quesson B, Desbarats P, Salomir R, Palussière J, Moonen CTW (2004) Atlas-Based Motion Correction For On-Line MR Temperature Mapping. IEEE ICIP 3:2571–2574

23. Gubjartsson H, Patz S (1995) The Rician distribution of noisy MRI data. Magn Reson Med 34:910–914

24. Goldberg SN, Gazelle GS, Compton CC, Mueller PR, Tanabe KK (2000) Treatment of intrahepatic malignancy with radiofrequency ablation: radiologic-pathologic correlation. Cancer 88:2452–2463

25. Pereira PL, Trubenbach J, Schenk M, Subke J, Kroeber S, Schaefer I, Remy CT, Schmidt D, Brieger J, Claussen CD (2004) Radiofrequency ablation: in vivo comparison of four commercially available devices in pig livers. Radiology 232:482–490

26. Wenneberg AE, Nalesnik MA, Coleman WB (1993) Hepatocyte paraffin 1 : a monoclonal antibody that reacts with hepatocytes and can be used for differential diagnosis of hepatic tumors. Am J Pathol 143:1050–1054

27. Bland JM, Altman DG (1986) Statistical methods for assessing agreement between two methods of clinical measurement. Lancet 1:307–310

28. Nour SG, Lewin JS (2005) Radiofrequency thermal ablation: the role of MR imaging in guiding and monitoring tumor therapy. Magn Reson Imaging Clin N Am 13:561–581

29. Lewin JS, Nour SG, Connell CF, Sulman A, Duerk JL, Resnick MI, Haaga JR (2004) Phase II clinical trial of interactive MR imaging-guided interstitial radiofrequency thermal ablation of primary kidney tumors: initial experience. Radiology 232:835–845

30. Lazebnik RS, Breen MS, Fitzmaurice M, Nour SG, Lewin JS, Wilson DL (2005) Radio-frequency-induced thermal lesions: subacute magnetic resonance appearance and histological correlation. J Magn Reson Imaging 18:487–495

31. Keserci BM, Kokuryo D, Suzuki K, Kumamoto E, Okada A, Khankan AA, Kuroda K (2006) Near-real-time feedback control system for liver thermal ablations based on self-referenced temperature imaging. Eur J Radiol 59:175–182

32. Young IR, Hand JW, Oatridge A, Prior MV (1994) Modeling and observation of temperature changes in vivo using MRI. Magn Reson Med 32:358–369

33. Kuroda K, Kokuryo D, Kumamoto E, Suzuki K, Matsuoka Y, Keserci B (2006) Optimization of self-reference thermometry using complex field estimation. Magn Reson Med 56:835–843

34. Stollberger R, Ascher PW, Huber D, Renhart W, Radner H, Ebner F (1998) Temperature monitoring of interstitial thermal tissue coagulation using MR phase images. J Magn Reson Imaging 8:188–196

35. Morimoto M, Sugimori K, Shirato K, Kokawa A, Tomita N, Saito T, Tanaka, N, Nozawa A, Hara M, Sekihara H, Shimada H, Imada T, Tanaka K (2002) Treatment of hepatocellular carcinoma with radiofrequency ablation: radiologic-histologic correlation during follow-up periods. Hepatology 35:1467–1475

36. Merkle EM, Nour SG, Lewin JS (2005) MR imaging follow-up after percutaneous radiofrequency ablation of renal cell carcinoma: findings in 18 patients during first 6 months. Radiology 235:1065–1071

37. Nour SG, Lewin JS, Gutman M, Hillenbrand C, Wacker FK, Wong JW, Mitchell IC, Armstrong CB, Hashim MM, Duerk JL, Strauss M (2004) Percutaneous MR imaging-guided radiofrequency interstitial thermal ablation of tongue base in porcine models: implications for obstructive sleep apnea syndrome. Radiology 230:359–368